

Analyzing Linear Stability of a Hypersonic Flow over Rotex-T Vehicle

Research Project

Author: Gilad Raz
Advisor: Prof. Vassilis Theofilis
Department of Aerospace Engineering
Technion – Israel Institute of Technology

Spring Semester 2025

Abstract

This project develops and validates a workflow for analyzing hypersonic boundary-layer instability over conical forebodies, with the ROTEX-T configuration as the longer-term target. An inviscid base solution is obtained by deriving and implementing the Taylor-Maccoll (TM) formulation and validating it against published cases across Mach number and cone half-angle. Viscous base flows are then computed in **OpenFOAM** on a one-cell-thick structured mesh with a finite-radius nose; grid independence is assessed via density-residual histories from multiple probes. The simulation is post-processed and then compared quantitatively with TM, with boundary-layer edge properties (M_e , T_e , U_e) showing close agreement. Additional checks include sampling along a ray between the boundary layer and the shock to verify consistency with conical similarity, and extracting velocity/temperature profiles to confirm expected boundary-layer behavior. In parallel, a proof-of-concept linear stability study solves the incompressible Orr-Sommerfeld problem for plane Poiseuille flow using Chebyshev collocation, validated by reproducing classical spectra and neutral conditions. Collectively, these steps establish a foundation for coupling viscous-compressible stability analysis to CFD-generated base flows. Future work will improve mesh refinement and extend the methodology to the geometry of ROTEX-T to assess instability mechanisms and transitions in realistic hypersonic configurations.

Nomenclature

Notation

t	Time
ρ	Density
p	Pressure
T	Static Temperature
L	Reference Length Scale
U	Velocity Magnitude
\mathbf{u}	Velocity Vector
u	Streamwise Velocity
v	Normal Velocity
w	Spanwise Velocity
λ	Second Viscosity Coefficient
μ	Dynamic Viscosity Coefficient
$\nu = \frac{\mu}{\rho}$	Kinematic Viscosity
γ	Specific Heat Ratio

κ	Heat Conductivity
c_p, c_v	Isobaric and Isochoric Heat Capacities
R_g	Specific Gas Constant
$\boldsymbol{\tau}$	Viscous Stress Tensor
Φ	Viscous Dissipation Tensor
δ	Cone Half-Angle
β	Shock Angle
α	Complex Wavenumber

Embellishments

$(\cdot)_\infty$	Reference Value (Far From Body)
$(\cdot)_e$	Boundary Layer Edge Value
$(\cdot)^*$	Dimensional Value
$(\cdot)'$	First Derivative
$(\cdot)''$	Second Derivative

1 Introduction

1.1 Literature Review

The prediction of laminar-turbulent transition in hypersonic flows remains a central challenge in high-speed aerodynamics. Transition to turbulent flow strongly influences surface heating, skin friction, and vehicle control authority, with even small shifts in location producing drastic changes in thermal protection requirements and aerodynamic performance. Understanding and accurately predicting the mechanisms that govern instability growth in hypersonic boundary layers is therefore essential for future vehicle design and safety (Schmisseur, 2015).

Laminar-turbulent transition seldom proceeds as a single abrupt event; rather, the roadmap of the laminar-turbulent boundary layer transition follows multiple paths: beginning with receptivity of the boundary layer to external disturbances, followed by linear (modal or nonmodal) amplification, nonlinear interactions and secondary instabilities, and culminating in breakdown to turbulent spots and their merger into a fully turbulent layer (Morkovin et al., 1994). Infinitesimal disturbances may decay or grow depending on the local stability characteristics of the mean flow, while finite-amplitude *bypass* routes may be triggered by freestream turbulence, surface roughness, or thermal effects. Predicting transition therefore requires identifying the dominant route and quantifying its receptivity and amplification to determine when and where breakdown will occur.

Instability in *supersonic compressible boundary layers* has been shown to be dominated by the *Mack modes* (Mack, 1969, 1984). The first, often regarded as the compressible continuation of the viscous instability discovered by Tollmien (Tollmien, 1929) and Schlichting (Schlichting, 1933), retains a vortical, shear-driven nature but becomes progressively stabilized as compressibility increases. In addition, at higher Mach numbers, typically beyond $M_\infty \approx 4$, the *second mode* appears—an acoustic-type instability that arises from the resonance of trapped waves between the wall and the sonic line and dominates transition in the hypersonic regime. Experiments on slender cones at zero angle of attack have consistently shown second-mode amplification to be the primary driver of transition under quiet freestream conditions, while wall temperature, nose bluntness, and freestream disturbances have been observed to modulate its growth rates (Stetson et al., 1983; Schneider, 2008). More recent reviews, such as that of Fedorov (Fedorov, 2011), provide a comprehensive synthesis of hypersonic boundary-layer instability physics, emphasizing the onset and dominance of the second mode at high Mach numbers, its sensitivity to thermal conditions, and the influence of high-enthalpy and real-gas effects.

To study the mechanism of instability, a hierarchy of stability analysis methods has been developed. Local Linear Stability Theory (LST) remains the most widely used and effective tool for analyzing hypersonic conical boundary-layer instabilities due to its balance between tractability and physical fidelity (Malik, 1990). More advanced frameworks, such as bi-global and tri-global analyses, relax the parallel-flow assumption and are capable of capturing non-parallelism, curvature, and fully three-dimensional effects; comprehensive reviews of such global approaches are provided by Theofilis (Theofilis, 2011).

In the present work, LST is adopted as the primary analytical framework, consistent with the restricted scope of analyzing the conical forebody of a hypersonic vehicle (e.g. ROTEX-T). This enables efficient characterization of instability mechanisms most relevant to hypersonic cone flows, while laying the groundwork for future studies in which global techniques will be applied to the full vehicle configuration.

1.2 Scope and Limitations

The present work is restricted to the conical forebody of a hypersonic vehicle at zero angle of attack. The outer flowfield is modeled under the assumption of *conical similarity*, with edge conditions of the Taylor–Maccoll solution later used to compare and validate viscous mean flows generated in OpenFOAM. Several simplifying assumptions are made:

- The gas is treated as *calorically perfect*, with constant γ and R_g .
- High-temperature effects, real-gas behavior, and finite-rate chemistry are neglected.
- The flow is assumed laminar up to the point of instability growth; nonlinear breakdown and transition to turbulence are not modeled.
- Freestream noise, wall roughness, and surface ablation or catalytic effects are not considered.

Within this framework, the results provide a baseline assessment of boundary-layer instability mechanisms on the cone. In

future studies, the analysis will be extended to the full vehicle configuration using global techniques capable of resolving non-parallel and three-dimensional effects.

2 Physical Problem

This study considers the external hypersonic flow over the axisymmetric conical forebody of a hypersonic vehicle (e.g. ROTEX-T) at zero angle of attack. The freestream satisfies $M_\infty \geq 5$; the gas is modeled as calorically perfect with Sutherland viscosity, and the wall (cone surface) is smooth, adiabatic, and no-slip.



Figure 1: ROTEX-T hypersonic vehicle model during roll-out (DLR, 2016) - conic forebody highlighted in red.

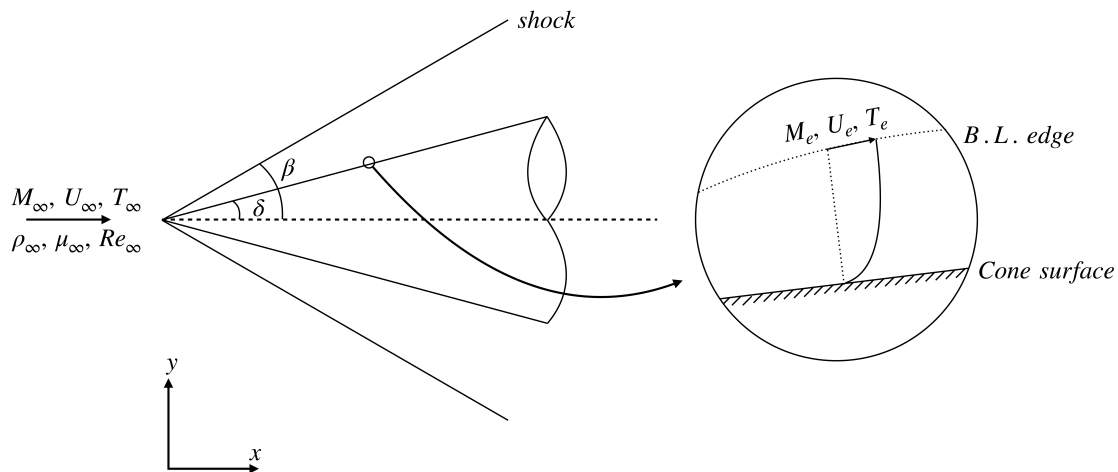


Figure 2: Conical forebody with straight shock (left) with zoomed in boundary layer schematic (right)

Away from the nose region, the flow admits conical similarity and a conical shock at angle β . The inviscid outer solution is obtained from CFD simulations and compared to the Taylor-Maccoll (TM) formulation, which supplies β and boundary-layer (BL) edge properties along rays of constant polar angle θ :

$$\{M_e(\theta), U_e(\theta), T_e(\theta), p_e(\theta)\}.$$

The present analysis focuses on downstream portions of the cone to avoid near-tip/bow-shock effects; TM predictions are used to verify the simulated shock angle and BL edge values. In the context of transition, these BL-edge fields define the reference state about which small disturbances may amplify (e.g., first- and second-mode mechanisms at hypersonic speeds).

3 Theoretical Background

3.1 Navier-Stokes Equations

Derived from the basic principles of conservation of mass, momentum, and energy, the Navier-Stokes equations (NSE) govern the motion of a compressible fluid. The underlying assumptions driving this model are:

- **Continuum Hypothesis:** The fluid is treated as a continuous medium, which may only be valid when the mean free path is small relative to the reference length scale (i.e. $Kn = \frac{\lambda}{L} \ll 1$).
- **Viscous, Newtonian Fluid:** The model accounts for internal friction within the fluid due to velocity gradients, characterized by a non-zero viscosity that is linearly proportional to the rate of strain tensor.
- **Stokes' Hypothesis:** The bulk viscosity is related to the dynamic viscosity by $\lambda = -\frac{2}{3}\mu$.
- **Calorically perfect gas (CPG):** c_p^* and c_v^* are constants with $\gamma = c_p^*/c_v^*$ is constant.

As such, the NSE (including equation of state), expressed in vector notation and a non-dimensional form, yield the following non-linear partial differential equations (PDEs):

$$\frac{\partial \rho}{\partial t} + \nabla \cdot (\rho \mathbf{u}) = 0 \quad (1a)$$

$$\rho \left[\frac{\partial \mathbf{u}}{\partial t} + (\mathbf{u} \cdot \nabla) \mathbf{u} \right] = -\nabla p + \frac{1}{Re} (\nabla \cdot \boldsymbol{\tau}) \quad (1b)$$

$$\rho c_p \left[\frac{\partial T}{\partial t} + (\mathbf{u} \cdot \nabla) T \right] = \frac{1}{Re Pr} \nabla \cdot (\kappa \nabla T) + (\gamma - 1) M^2 \left[\frac{\partial p}{\partial t} + (\mathbf{u} \cdot \nabla) p + \frac{1}{Re} \Phi \right] \quad (1c)$$

$$p = \frac{\rho T}{\gamma M^2} \quad (1d)$$

Where the viscous stress tensor $\boldsymbol{\tau}$, and viscous dissipation Φ are respectively defined as follows:

$$\boldsymbol{\tau} = \mu [\nabla \mathbf{u} + (\nabla \mathbf{u})^T] - \frac{2}{3} \mu (\nabla \cdot \mathbf{u}) \mathbf{I} \quad (2a)$$

$$\Phi = \lambda (\nabla \cdot \mathbf{u})^2 + \frac{1}{2} \mu [\nabla \mathbf{u} + (\nabla \mathbf{u})^T]^2 \quad (2b)$$

The principal non-dimensional parameters characterizing the flow field are the *Mach*, *Prandtl* and *Reynolds*, and are respectively defined as follows:

$$M = \frac{U_\infty^*}{\sqrt{R_g \gamma T_\infty^*}} \quad ; \quad Pr = \frac{\mu_\infty^* c_{p,\infty}^*}{\kappa_\infty^*} \quad ; \quad Re = \frac{U_\infty^* L^*}{\nu_\infty^*} \quad (3)$$

The flow and material quantities presented in Eqns. (1a)–(1d) have been non-dimensionalized in the following manner:

$$\mathbf{u} = \frac{\mathbf{u}^*}{U_\infty^*}, \quad t = \frac{t^* U_\infty^*}{L^*}, \quad p = \frac{p^*}{\rho U_\infty^{*2}}, \quad \rho = \frac{\rho^*}{\rho_\infty}, \quad T = \frac{T^*}{T_\infty} \quad (4a)$$

$$\mu = \frac{\mu^*}{\mu_\infty}, \quad \kappa = \frac{\kappa^*}{\kappa_\infty}, \quad c_p = \frac{c_p^*}{c_{p,\infty}^*} \stackrel{\text{CPG}}{=} 1, \quad \nabla = \nabla^* L^* \quad (4b)$$

3.2 NSE – Spherical Coordinates (Axisymmetric)

This section will analyze steady, compressible flow past a slender circular cone at zero angle of attack and recast the Navier–Stokes system of Sec. 3.1 in spherical coordinates (r, θ, ϕ) while preserving the non-dimensional scaling.

The spherical coordinate system (r, θ, ϕ) is defined as:

- r is the radial distance from the origin (cone apex),
- θ is the polar angle measured from the axis of symmetry,
- ϕ is the azimuthal angle (around the cone).

Under the assumption of axisymmetry (no dependence on ϕ : $\partial/\partial\phi = 0$), the velocity field is:

$$\mathbf{u}(r, \theta) = u_r(r, \theta)\hat{\mathbf{e}}_r + u_\theta(r, \theta)\hat{\mathbf{e}}_\theta \quad ; \quad u_\phi = 0 \quad (5)$$

Continuity Equation

$$\frac{1}{r^2} \frac{\partial}{\partial r}(r^2 \rho u_r) + \frac{1}{r \sin \theta} \frac{\partial}{\partial \theta}(\rho u_\theta \sin \theta) = 0 \quad (6)$$

Radial (\hat{r}) Momentum Equation

$$\rho \left(u_r \frac{\partial u_r}{\partial r} + \frac{u_\theta}{r} \frac{\partial u_r}{\partial \theta} - \frac{u_\theta^2}{r} \right) = -\frac{\partial p}{\partial r} + \frac{1}{Re} (\nabla \cdot \boldsymbol{\tau}) \cdot \hat{\mathbf{e}}_r \quad (7)$$

Polar ($\hat{\theta}$) Momentum Equation

$$\rho \left(u_r \frac{\partial u_\theta}{\partial r} + \frac{u_\theta}{r} \frac{\partial u_\theta}{\partial \theta} + \frac{u_r u_\theta}{r} \right) = -\frac{1}{r} \frac{\partial p}{\partial \theta} + \frac{1}{Re} (\nabla \cdot \boldsymbol{\tau}) \cdot \hat{\mathbf{e}}_\theta \quad (8)$$

Azimuthal ($\hat{\phi}$) Momentum Equation - Satisfied by the assumption of axisymmetry: $\frac{\partial}{\partial\phi} = u_\phi = 0$.

Energy Equation

$$\rho c_p \left(u_r \frac{\partial T}{\partial r} + \frac{u_\theta}{r} \frac{\partial T}{\partial \theta} \right) = \frac{1}{Re Pr} \left[\frac{1}{r^2} \frac{\partial}{\partial r} \left(r^2 \kappa \frac{\partial T}{\partial r} \right) + \frac{1}{r^2 \sin \theta} \frac{\partial}{\partial \theta} \left(\kappa \sin \theta \frac{\partial T}{\partial \theta} \right) \right] + (\gamma - 1) M^2 \left(u_r \frac{\partial p}{\partial r} + \frac{u_\theta}{r} \frac{\partial p}{\partial \theta} + \frac{1}{Re} \Phi \right) \quad (9)$$

Dissipation Function

$$\Phi = \lambda \left(\frac{1}{r^2} \frac{\partial}{\partial r} (r^2 u_r) + \frac{1}{r \sin \theta} \frac{\partial}{\partial \theta} (u_\theta \sin \theta) \right)^2 + \mu \left[\left(\frac{\partial u_r}{\partial r} \right)^2 + \left(\frac{1}{r} \frac{\partial u_\theta}{\partial \theta} + \frac{u_r}{r} \right)^2 + \frac{1}{r^2} \left(\frac{\partial u_\theta}{\partial \theta} - u_\theta \cot \theta \right)^2 \right] \quad (10)$$

3.3 Conical Similarity

In addition to axisymmetry ($\partial/\partial\phi = 0$), due to the cone geometry we adopt **conical similarity**¹ ($\partial/\partial r = 0$), such that under conical flow all variables depend only on the polar angle θ :

$$\psi(r, \theta, \phi) = \psi(\theta) \quad ; \quad \frac{\partial \psi}{\partial \theta} = \frac{d\psi}{d\theta} \quad (11)$$

Accordingly, the velocity field reduces to:

$$\mathbf{u}(\theta) = u_r(\theta) \hat{\mathbf{e}}_r + u_\theta(\theta) \hat{\mathbf{e}}_\theta \quad (12)$$

¹This assumption is appropriate for slender cones with an attached conical shock, where the inviscid region outside the (thin) boundary layer is dominant. Conical similarity does *not* describe the viscous boundary layer (BL) near the wall, where gradients normal to the surface are large and viscous terms are $\mathcal{O}(1/Re)$. Accordingly, the Taylor–Maccoll formulation derived below provides a baseline comparison for the *outer inviscid solution and edge conditions* for the BL, but is not a BL solution itself.

Continuity Equation

$$2u_r + u_\theta \cot \theta + \frac{du_\theta}{d\theta} + \frac{u_\theta}{\rho} \frac{d\rho}{d\theta} = 0 \quad (13)$$

Radial Momentum Equation

$$\rho \left(\frac{u_\theta}{r} \frac{du_r}{d\theta} - \frac{u_\theta^2}{r} \right) = -\frac{dp}{dr} + \frac{1}{Re} (\nabla \cdot \boldsymbol{\tau}) \cdot \hat{\mathbf{e}}_r \quad (14)$$

Where the radial component of the viscous force becomes ($\lambda + \frac{2}{3}\mu = 0$):

$$(\nabla \cdot \boldsymbol{\tau}) \cdot \hat{\mathbf{e}}_r = \frac{1}{r^2} \frac{d}{d\theta} \left[\mu \left(\frac{1}{\sin \theta} \frac{d}{d\theta} (u_r \sin \theta) \right) \right] - \frac{2\mu}{r^2} \left(u_r - \frac{1}{\sin \theta} \frac{d}{d\theta} (u_\theta \sin \theta) \right) \quad (15)$$

Polar Momentum Equation

$$\rho \left(\frac{u_\theta}{r} \frac{du_\theta}{d\theta} + \frac{u_r u_\theta}{r} \right) = -\frac{1}{r} \frac{dp}{d\theta} + \frac{1}{Re} (\nabla \cdot \boldsymbol{\tau}) \cdot \hat{\mathbf{e}}_\theta \quad (16)$$

Where the polar component of the viscous force becomes:

$$(\nabla \cdot \boldsymbol{\tau}) \cdot \hat{\mathbf{e}}_\theta = \frac{\mu}{r^2} \left[\frac{d^2 u_\theta}{d\theta^2} + \cot \theta \frac{du_\theta}{d\theta} - \frac{u_\theta}{\sin^2 \theta} + 2 \frac{du_r}{d\theta} - 2u_\theta \right] \quad (17)$$

Energy Equation

$$\rho c_p \left(\frac{u_\theta}{r} \frac{dT}{d\theta} \right) = \frac{1}{RePr} \cdot \frac{1}{r^2 \sin \theta} \frac{d}{d\theta} \left(\kappa \sin \theta \frac{dT}{d\theta} \right) + (\gamma - 1) M^2 \left(\frac{u_\theta}{r} \frac{dp}{d\theta} + \frac{1}{Re} \Phi \right) \quad (18)$$

Dissipation Function

$$\Phi = \lambda \left(\frac{2u_r}{r} + \frac{1}{r \sin \theta} \frac{d}{d\theta} (u_\theta \sin \theta) \right)^2 + \mu \left[\left(\frac{1}{r} \frac{du_\theta}{d\theta} + \frac{u_r}{r} \right)^2 + \frac{1}{r^2} \left(\frac{du_\theta}{d\theta} - u_\theta \cot \theta \right)^2 \right] \quad (19)$$

3.4 Inviscid Flow

In the high-Reynolds-number limit the viscous stresses are confined to a thin boundary layer near the wall, while the outer region is accurately modeled as inviscid. In this *outer* region the viscous terms scale as $\mathcal{O}(1/Re)$, thus as $Re \rightarrow \infty$:

$$\frac{1}{Re} (\nabla \cdot \boldsymbol{\tau}) \cdot \hat{\mathbf{e}}_r \rightarrow 0 \quad ; \quad \frac{1}{Re} (\nabla \cdot \boldsymbol{\tau}) \cdot \hat{\mathbf{e}}_\theta \rightarrow 0 \quad ; \quad \frac{1}{Re} \Phi \rightarrow 0 \quad (20)$$

The conical-similarity form above then reduces the outer region to ordinary differential equations in θ , with the resulting system describing an inviscid, compressible, conical flow field. The inviscid continuity, momentum (polar and radial, respectively), energy, and state equations are:

$$\text{Continuity:} \quad 2u_r + u_\theta \cot \theta + \frac{du_\theta}{d\theta} + \frac{u_\theta}{\rho} \frac{d\rho}{d\theta} = 0 \quad (21a)$$

$$\text{Radial momentum:} \quad \rho \left(\frac{u_\theta}{r} \frac{du_r}{d\theta} - \frac{u_\theta^2}{r} \right) = -\frac{dp}{dr} \quad (21b)$$

$$\text{Polar momentum:} \quad \rho \left(\frac{u_\theta}{r} \frac{du_\theta}{d\theta} + \frac{u_r u_\theta}{r} \right) = -\frac{1}{r} \frac{dp}{d\theta} \quad (21c)$$

$$\text{Energy:} \quad \rho c_p \left(\frac{u_\theta}{r} \frac{dT}{d\theta} \right) = (\gamma - 1) M^2 \left(\frac{u_\theta}{r} \frac{dp}{d\theta} \right) \quad (21d)$$

$$\text{State:} \quad p = \frac{\rho T}{\gamma M^2} \quad (21e)$$

3.5 Derivation of the Taylor-Maccoll Equation

Finally, treating the flow in the shock-cone layer as steady, inviscid, adiabatic, axisymmetric, and conically self-similar, the Taylor-Maccoll velocity representation, only dependent on θ , is introduced:

$$u_r(\theta) = V \cos \psi, \quad u_\theta(\theta) = -V \sin \psi \quad (22)$$

Where: $V = V(\theta)$ is the local non-dimensional velocity magnitude, and $\psi = \psi(\theta)$ is the angle between the velocity vector (\mathbf{u}) and the radial direction ($\hat{\mathbf{e}}_r$).

Given the defined velocity relations:

$$\frac{du_r}{d\theta} = V' \cos \psi - V \psi' \sin \psi \quad ; \quad \frac{du_\theta}{d\theta} = -V' \sin \psi - V \psi' \cos \psi \quad ; \quad (\cdot)' = \frac{d(\cdot)}{d\theta} \quad (23)$$

Substituting u_r, u_θ and their respective derivatives into (21b)–(21c) and simplifying yields:

$$-\frac{dp}{d\theta} = \rho \left[(-V \sin \psi)(V' \sin \psi - V \psi' \cos \psi) + (V \cos \psi)(-V \sin \psi) \right] = \rho \left[VV' \sin^2 \psi + V^2 \sin \psi \cos \psi (\psi' - 1) \right] \quad (24a)$$

$$-r \frac{dp}{dr} = 0 = \rho \left[(-V \sin \psi)(V' \cos \psi - V \psi' \sin \psi) - (-V \sin \psi)^2 \right] = \rho \left[-VV' \sin \psi \cos \psi + V^2 \sin^2 \psi (\psi' - 1) \right] \quad (24b)$$

conic sim.

Dividing (24b) by $V^2 \sin \psi \cos \psi$ respectively yields the following kinematic relation and streamwise identity:

$$\frac{V'}{V} = \tan \psi (\psi' - 1) \implies -\frac{1}{\rho} \frac{dp}{d\theta} = V^2 (\psi' - 1) (\tan \psi \sin^2 \psi \sin \psi \cos \psi) = V^2 (\psi' - 1) \tan \psi = VV' \quad (25)$$

Furthermore, the continuity equation in V, ψ form is simplified to:

$$\frac{1}{\rho} \frac{d\rho}{d\theta} = 2 \cot \psi - \cot \theta - \frac{V'}{V} - \psi' \cot \psi \quad (26)$$

To close the system, isentropic relations for steady, inviscid, adiabatic flow are invoked:

$$\frac{1}{p} \frac{dp}{d\theta} = \gamma \frac{1}{\rho} \frac{d\rho}{d\theta} \quad ; \quad a^2 = \frac{\gamma p}{\rho} \quad ; \quad M^2 = \frac{V^2}{a^2} = \frac{\rho V^2}{\gamma p} \quad (27)$$

Together with the kinematic identity $\frac{V'}{V} = \tan \psi (\psi' - 1)$ from (25) and continuity (26), this yields:

$$\frac{1}{p} \frac{dp}{d\theta} = \gamma M^2 \tan \psi (1 - \psi') = \gamma \frac{1}{\rho} \frac{d\rho}{d\theta} \implies -\frac{1}{\rho V^2} \frac{dp}{d\theta} = (\psi' - 1) \tan \psi \quad (28)$$

Rearranging:

$$M^2 \tan \psi (1 - \psi') = 2 \cot \psi - \cot \theta - \tan \psi (\psi' - 1) - \psi' \cot \psi \quad (29)$$

By defining $H(\theta) = \frac{1}{\rho V^2}$, $-\frac{1}{\rho V^2} \frac{dp}{d\theta}$ may be differentiated with respect to θ :

$$-Hp'' - H'p' = \psi'' \tan \psi + (\psi' - 1) \sec^2 \psi \psi' \quad (30)$$

Expressing the relevant derivatives:

$$H' = -H \left(\frac{\rho'}{\rho} + 2 \frac{V'}{V} \right) \quad ; \quad \frac{\rho'}{\rho} = \frac{1}{\rho} \frac{d\rho}{d\theta} \implies \frac{\rho'}{\rho} + 2 \frac{V'}{V} = 2 \cot \psi - \cot \theta - \psi' \cot \psi + \tan \psi (\psi' - 1) \quad (31)$$

The derivatives p' and p'' are given by isentropic relations:

$$p' = \frac{dp}{d\theta} = a^2 \frac{\rho'}{\rho} = \frac{V^2}{M^2} \frac{\rho'}{\rho} \quad ; \quad p'' = \frac{V^2}{M^2} \left[\left(\frac{\rho'}{\rho} \right)' + \left(2 \frac{V'}{V} - \frac{(M^2)'}{M^2} \right) \frac{\rho'}{\rho} \right] \quad (32)$$

Substituting the above expressions into (30) and simplifying provides the celebrated Taylor-Maccoll equation:

$$\boxed{(1 - M^2)(\psi'' + \cot \theta \psi') + 2M^2 \sin \psi \cos \psi = 0} \quad (33)$$

3.5.1 Relation between $M(\theta)$ & $\psi(\theta)$:

Noting that the Taylor-Maccoll ODE seems to contain two variables, $M(\theta)$, $\psi(\theta)$ and only one equation with which to resolve the problem, it is vital to express the direct relationship between the two variables and thus provide closure. Further arithmetic on (29) yields the direct relation between the Mach number and $\psi(\theta)$:

$$M^2(\theta) = \frac{\psi' \tan \psi + \psi' \cot \psi - 2 \cot \psi + \cot \theta - \tan \psi}{\tan \psi (\psi' - 1)} \quad (34)$$

Note: In what follows, the Taylor-Maccoll solution supplies the edge (outer) state and shock geometry that will be used to validate the viscous mean-flow profiles extracted from the `OpenFOAM` simulation.

4 Linear Stability Theory

4.1 Linearized Navier-Stokes Equations

The linear stability analysis of the flow is based on the non-dimensionalized NSE [Eqns.(1)-(3)]. With the fluid's primitive state variables defined as:

$$\mathbf{q} = \begin{bmatrix} \rho \\ u \\ v \\ w \\ T \end{bmatrix} \quad (35)$$

Thus, we can decompose the state variables into a *steady base-flow* (obtained via an OpenFOAM simulation) and *unsteady small-amplitude perturbations*:

$$\mathbf{q}(\mathbf{x}, t) = \bar{\mathbf{q}}(\mathbf{x}) + \epsilon \tilde{\mathbf{q}}(\mathbf{x}, t) \quad , \quad \epsilon \ll 1 \quad ; \quad \bar{\mathbf{q}} = \begin{bmatrix} \bar{\rho} \\ \bar{u} \\ \bar{v} \\ \bar{w} \\ \bar{T} \end{bmatrix} \quad ; \quad \tilde{\mathbf{q}} = \begin{bmatrix} \tilde{\rho} \\ \tilde{u} \\ \tilde{v} \\ \tilde{w} \\ \tilde{T} \end{bmatrix} \quad ; \quad \mathbf{x} = \begin{bmatrix} x \\ y \\ z \end{bmatrix} \quad (36)$$

Where: vector \mathbf{x} defines the fluid's coordinates **within the boundary layer**, with x streamwise, y wall-normal, and z spanwise.

By subtracting the 'pure' baseflow terms [$\mathcal{O}(1)$] and neglecting higher order terms such as $\mathcal{O}(\epsilon^2)$ and above, we arrive at $\mathcal{O}(\epsilon)$ equations which are the **Linearized Navier-Stokes Equations** (LNSE). For the sake of brevity, in the incompressible limit, the LNSE for continuity and momentum are expressed as:

$$\nabla \cdot \tilde{\mathbf{u}} = 0 \quad (37)$$

$$\frac{\partial \tilde{\mathbf{u}}}{\partial t} + \bar{\mathbf{u}} \cdot \frac{2u_r}{r} \tilde{\mathbf{u}} + \tilde{\mathbf{u}} \cdot \nabla \bar{\mathbf{u}} = -\frac{2u_r}{r} p + \frac{1}{Re} \frac{2u_r^2}{r} \tilde{\mathbf{u}} \quad (38)$$

4.2 Local Linear Stability Analysis (LST)

In local linear stability analysis the base flow is assumed to be *locally parallel*: it varies only in a single inhomogeneous direction, while being homogeneous in the others. In the hypersonic cone case, at zero angle of attack, the axisymmetric geometry and conical similarity of the base flow are invoked. As such, the base flow can be represented in a local Cartesian frame where x is the streamwise direction, y is the wall-normal direction, and z is treated as the spanwise direction. In this framework, the base flow depends only on y , while modal perturbations are expressed using the following Fourier ansatz:

$$\tilde{q}(x, y, z, t) = \hat{q}(y) e^{i(\alpha x + \beta z - \omega t)} \quad (39)$$

Where: $\hat{q}(y)$ is the wall-normal eigenfunction, $\alpha = \frac{2\pi}{L_x}$ is the streamwise wavenumber, $\beta = \frac{2\pi}{L_z}$ is the spanwise wavenumber, L_x, L_z are the periodicity lengths along the homogeneous directions x, z respectively and ω is the complex angular frequency.

Furthermore, the above ansatz can now be substituted into the incompressible LNSE [eqns.(37)-(38)] to produce the following system of equations:

$$\begin{aligned}
\mathcal{L}\hat{u} + \bar{u}_y\hat{v} + i\alpha\hat{p} &= 0 \\
\mathcal{L}\hat{v} + \hat{p}_y &= 0 \\
\mathcal{L}\hat{w} + \bar{w}_y\hat{v} - i\beta\hat{p} &= 0 \\
i\alpha\hat{u} + \hat{v}_y + \hat{w}_z &= 0
\end{aligned}
; \quad \mathcal{L} = i\alpha\bar{u} + i\beta\bar{w} - \frac{1}{Re} (D_{yy}^2 - \beta^2 - \alpha^2) - i\omega \tag{40}$$

Note: the compressible version of the above system of equations [eq.(40)], can be found in published literature (Malik, 1990).

4.3 Temporal Local Stability Formulation

Substitution of the Fourier ansatz into the LNSE reduces the governing equations to a generalized EVP of the form:

$$\mathcal{A}\hat{\mathbf{q}} = \omega\mathcal{B}\hat{\mathbf{q}}, \tag{41}$$

where \mathcal{A} and \mathcal{B} are linear operators depending on the base flow $\bar{\mathbf{q}}(y)$, the Reynolds number, and the chosen wavenumbers (α, β) . The eigenvector $\hat{\mathbf{q}}(y)$ represents the wall-normal structure of the disturbance, while the corresponding complex eigenvalue $\omega = \omega_r + i\omega_i$ encodes both the temporal frequency (ω_r) and the amplification or damping rate (ω_i) .

The solution of (41) provides the set of eigenvalues $\omega_j = \omega_{r,j} + i\omega_{i,j}$ and eigenfunctions $\hat{\mathbf{q}}_j(y)$. The temporal stability of the base flow is then determined according to the sign of the imaginary part ω_i . The marginal condition $\omega_i = 0$ defines a *neutral curve* in parameter space (Re, α, β) , with unstable disturbances ($\omega_i > 0$) defined as inside the curve and stable modes ($\omega_i < 0$) on the outside. Importantly, temporal and spatial formulations of linear stability *coincide* on this neutral boundary ($\omega_i = 0 \Leftrightarrow \alpha_i = 0$), which justifies the use of temporal analysis to trace the stability envelope.

In the incompressible limit, these operators take matrix form:

$$\mathcal{A} = \begin{pmatrix} \mathcal{L}_T & \bar{u}_y & 0 & i\alpha \\ 0 & \mathcal{L}_T & 0 & D_y \\ 0 & \bar{w}_y & \mathcal{L}_T & i\beta \\ i\alpha & D_y & i\beta & 0 \end{pmatrix} ; \quad \mathcal{B} = \begin{pmatrix} i & 0 & 0 & 0 \\ 0 & i & 0 & 0 \\ 0 & 0 & i & 0 \\ 0 & 0 & 0 & 0 \end{pmatrix} \tag{42}$$

Where:

$$\mathcal{L}_T = i\alpha\bar{u} + i\beta\bar{w} - \frac{1}{Re} (D_{yy}^2 - \alpha^2 - \beta^2). \tag{43}$$

4.4 Mapping Cartesian to Curvilinear Coordinates

For sake of brevity, the preceding formulation of the local stability problem was expressed for the incompressible limit in a Cartesian coordinate system (x, y, z) , with x streamwise, y wall-normal, and z spanwise. In the case of a hypersonic flow over a cone, the local stability approach is taken via the axisymmetry and conical similarity assumption (locally parallel along \hat{x}, \hat{z}), where only the inhomogeneous wall-normal direction is mapped, while the homogeneous streamwise and spanwise directions are left unchanged. Denoting the physical wall-normal coordinate by η and the standard collocation domain by ξ , the mapping $\eta = \eta(\xi)$ modifies the derivative operators as follows(González, 2014):

$$\hat{D}_{k,j}^1(\eta) = \frac{d\xi}{d\eta} D_{k,j}^1(\xi), \tag{44}$$

$$\hat{D}_{k,j}^2(\eta) = \left(\frac{d\xi}{d\eta}\right)^2 D_{k,j}^2(\xi) + \frac{d^2\xi}{d\eta^2} D_{k,j}^1(\xi). \tag{45}$$

Where: D^1 and D^2 are the first and second derivative matrices in the standard domain, while \hat{D}^1 and \hat{D}^2 are the corresponding operators in the physical domain.

5 Numerical Methodology

5.1 Taylor-Maccoll Solver - Shooting Method

To solve the Taylor–Maccoll equation numerically, the second-order ODE is recast as a system of two coupled first-order equations:

$$\begin{cases} \frac{d\bar{u}_r}{d\theta} = \bar{u}_\theta \\ \frac{d\bar{u}_\theta}{d\theta} = f(\bar{u}_r, \bar{u}_\theta, \theta) \end{cases} \quad (46)$$

Here, the function f is derived from rearranging the Taylor–Maccoll equation derived for the normalized radial velocity component, $u_r(\theta)$, and isolating the second derivative terms. The system is then integrated numerically using a *Runge–Kutta 4th-order (RK4) scheme*, marching inward from the shock angle $\theta = \theta_s$ to the cone surface $\theta = \delta$. Although $\bar{u}_r(\theta_s)$ is known from the post-shock velocity, the correct initial slope $\bar{u}_\theta(\theta_s)$ may not be obtained by inference. To resolve this, a shooting method is employed: an initial guess for $\bar{u}_\theta(\theta_s)$ is made, and the RK4 integrator is applied. The computed value of $\bar{u}_\theta(\delta)$ is then compared to the physical boundary condition at the cone surface:

$$\bar{u}_\theta(\delta) = 0 \quad (47)$$

If the boundary condition is not met, the initial guess is refined using the *bisection* root-finding algorithm, to minimize the residual at the cone surface:

$$|\bar{u}_\theta(\delta)| < \varepsilon \quad (48)$$

This iterative process continues until convergence is achieved. The result is a consistent solution $\bar{u}_r(\theta)$ and $\bar{u}_\theta(\theta)$ that satisfies both the shock entry conditions and the no-transverse-velocity boundary condition at the cone surface, fully resolving the inviscid, axisymmetric, conical flowfield.

5.2 3D Mesh & OpenFoam Solver Configuration

5.2.1 Computational Grid

A one-cell-thick three-dimensional structured mesh was constructed to represent the axisymmetric conical geometry with a blunt nose. The nose region occupies 1/39 of the total cone length and is defined as a circular arc smoothly tangent to the conical surface. The grid is refined towards both the blunt tip and the cone surface to capture the steep gradients near the wall and in the shock layer. The azimuthal thickness of one cell enforces axisymmetry while enabling the use of the three-dimensional compressible solver. Boundary conditions were assigned as follows: the cone surface as a `wall`, the two azimuthal faces as `wedge`, and the inflow and outflow planes as `patch` boundaries.

5.2.2 Solver and Numerical Setup

The simulations were performed using the `rhoCentralFoam` solver in OpenFOAM v2506. This density-based, second-order finite-volume solver integrates the compressible NSE using a central-upwind schemes of Kurganov and Tadmor with explicit time advancement. The flow was modeled as laminar and governed by the perfect-gas equation of state with Sutherland viscosity.

5.2.3 Discretization and Linear Solvers

Spatial and temporal discretization were defined by the `fvSchemes` and `fvSolution` dictionaries. A first-order Euler time scheme was employed, and all gradients, divergences, and Laplacians were evaluated with linear Gauss interpolation. Flux reconstruction used total-variation-diminishing van Leer limiters to maintain accuracy near discontinuities.

5.2.4 Probes and Data Sampling

Ten equidistant probes were placed along a straight ray extending from the arc-cone junction into the outer flow. Each probe recorded temporal variations of ρ, T, U during the computation. These data sets were used to evaluate local residual convergence and to compare edge values with the inviscid Taylor–Maccoll predictions.

6 Results

6.1 TM Numerical Solver Validation

To verify the accuracy and reliability of the T–M numerical solver (Pezlar, 2024) presented, validation was undertaken using selected freestream conditions and cone half–angles reported in the literature. As such, the solver’s predictions for the freestream parameters were juxtaposed against the published Taylor–Maccoll solutions (Dylewicz, 2025).

Note: the solver and thus, the results, were computed assuming constant heat capacity ratio, $\gamma = 1.4$ and gas constant, $R_g = 287.058 \left[\frac{J}{kg \cdot K} \right]$.

Case 1 - $M_\infty = 8$ & $\delta = 7^\circ$

In this case, the relevant free-stream flow parameters for the cone are :

M_∞	$p_\infty [Pa]$	$\rho_\infty [kg/m^3]$	$T_\infty [K]$
8	383.78	0.0246	54.35

Table 1: Free-stream flow parameters - (Kufner and Dallmann, 1995)

The corresponding computed boundary layer edge values (published Taylor-Maccoll solutions will be denoted as $TM_{lit.}$):

	M_e	$p_e [Pa]$	$\rho_e [kg/m^3]$	$T_e [K]$
$TM_{lit.}$	6.83	1001.16	0.04808	72.53
TM_{solver}	6.83	1003.76	0.04817	72.60

Table 2: Flow conditions at boundary layer edge for $M_\infty = 8$ & $\delta = 7^\circ$ cone - solver and literature comparison

Case 2 - $M_\infty = 5.7$ & $\delta = 7^\circ$

In this case, the relevant free-stream flow parameters for the cone are :

M_∞	$p_\infty [Pa]$	$\rho_\infty [kg/m^3]$	$T_\infty [K]$
5.7	426.62	0.0255	58.282

Table 3: Free-stream flow parameters (Davami et al., 2024)

The corresponding computed boundary layer edge values (published Taylor-Maccoll solutions will be denoted as $TM_{lit.}$):

	M_e	$p_e [Pa]$	$\rho_e [kg/m^3]$	$T_e [K]$
$TM_{lit.}$	5.11397	808.23	0.04014	70.14
TM_{solver}	5.11637	806.13	0.04007	70.08

Table 4: Flow conditions at boundary layer edge for $M_\infty = 6$ & $\delta = 7^\circ$ cone - solver and literature comparison

Numerical Solver Validity

Although the results obtained from the presented T–M numerical solver are not an exact match to the published values from Kamil’s solver, they are quite a close match. Minor differences can arise due to factors such as iteration precision, step-size handling in the Runge-Kutta integration, and numerical round-off. Additionally, Kamil’s published values may have been rounded off either as inputs or for clarity, meaning that even small discrepancies may stem from input or presentation choices rather than fundamental differences in solution method or accuracy. Overall, the close proximity between the solutions validates the accuracy and reliability of the presented T–M solver and its underlying methodology.

6.2 Base Flow – Grid Independence

To eliminate mesh resolution as a potential source of error affecting the accuracy and reliability of the results, a grid independence study was conducted. The same simulation setup was repeated for meshes of increasing resolution under *no-slip* wall boundary conditions. Verification of grid independence was performed by examining the temporal convergence of the density residual, defined as:

$$\text{Residual} = \frac{|\rho(t) - \rho_{\text{final}}|}{\rho_{\text{max}}} \quad (49)$$

Three mesh resolutions with progressively increasing grid densities were tested: Mesh 1 ($\sim 2\text{K}$ points), Mesh 2 ($\sim 20\text{K}$ points), and Mesh 3 ($\sim 200\text{K}$ points). The residuals were evaluated at two distinct probe locations within the domain to ensure that the assessment was not biased by local regions exhibiting faster or more favorable convergence behavior - probe 2 (near cone nose) and probe 9 (near outflow).

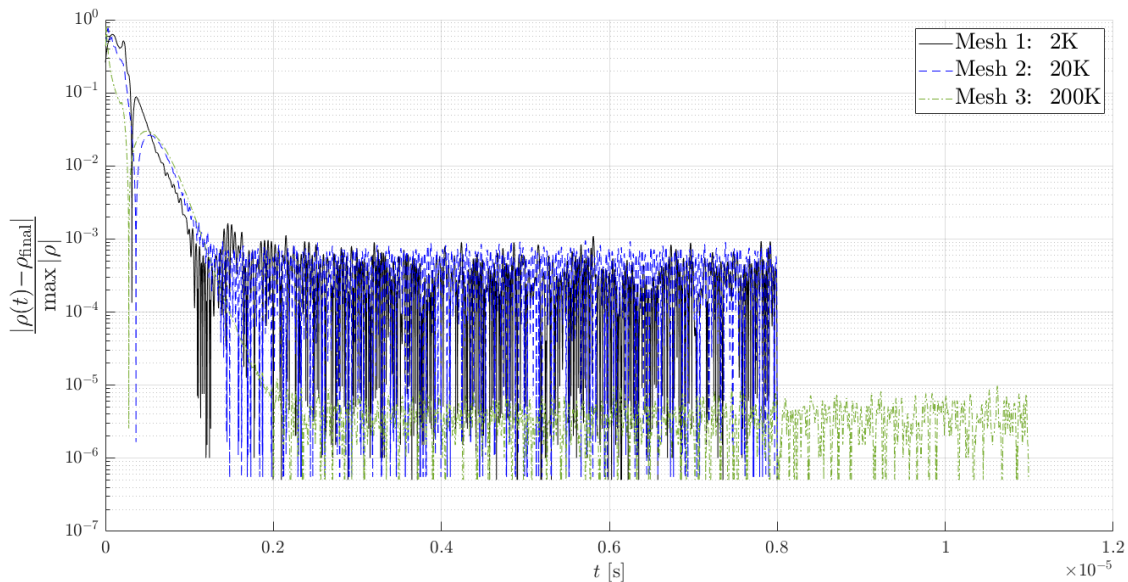


Figure 3: ρ Residual - Probe 2 (No Slip)

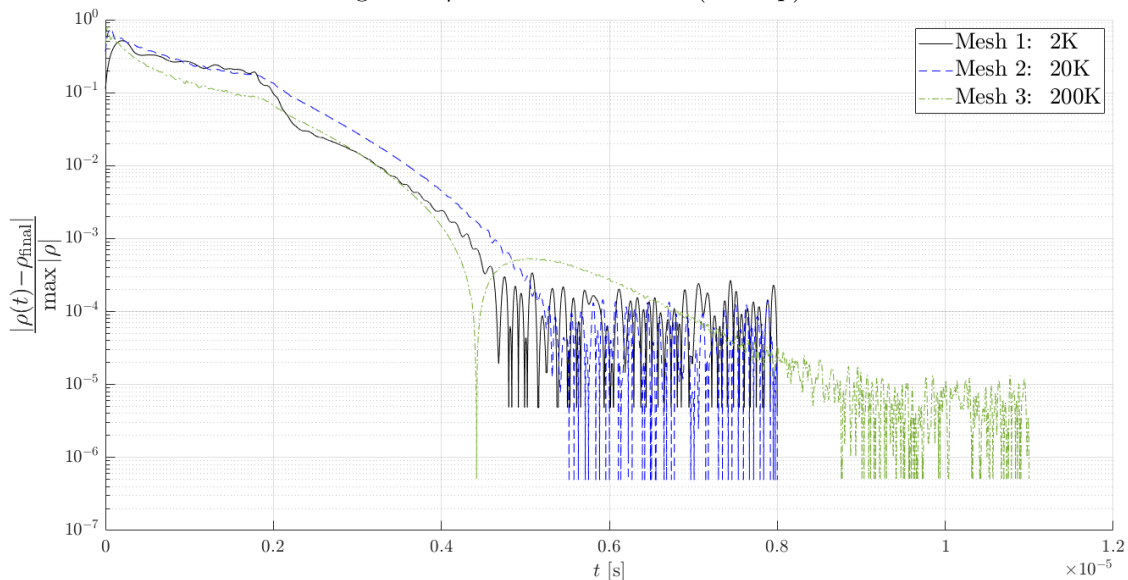


Figure 4: ρ Residual - Probe 9 (No Slip)

	Probe 2	$\Delta Res.$	Probe 9	$\Delta Res.$
Mesh 1	$2.998 \cdot 10^{-5}$	—	$1.895 \cdot 10^{-5}$	—
Mesh 2	$1.221 \cdot 10^{-5}$	$1.777 \cdot 10^{-5}$	$4.428 \cdot 10^{-6}$	$1.452 \cdot 10^{-5}$
Mesh 3	$2.050 \cdot 10^{-6}$	$1.016 \cdot 10^{-5}$	$2.561 \cdot 10^{-6}$	$1.867 \cdot 10^{-6}$

Table 5: Mean Converged Residual

6.3 Base-Flow Validation

6.3.1 Comparison to TM Solver Results

Establishing the base-flow’s spatial and temporal convergence now enables further validation via comparison to well-validated theoretical results. This comparison will be accomplished by implementing the verified TM solver as the baseline results with which the **OpenFOAM** simulation results will be compared against.

Although the simulated base flow includes viscous effects while the TM formulation assumes inviscid flow, this comparison remains crucial. The TM solution provides the most rigorous analytical description available for steady, compressible, axisymmetric flow over a conical surface with a straight attached shock, and thus serves as an essential theoretical benchmark for assessing the overall correctness of the computed shock geometry and outer-flow behavior.

The free-stream flow parameters input into the TM solver and **OpenFOAM** simulation are as tabulated below:

M_∞	$\delta[deg]$	$U_\infty [\frac{m}{s}]$	$T_\infty[K]$	$p_\infty [Pa]$	$\rho_\infty [\frac{kg}{m^3}]$	$\mu_\infty [\frac{kg}{m \cdot s}]$	$Re_\infty [\frac{1}{m}]$
5.002	6.2°	1002	100	$3.516 \cdot 10^4$	1.225	$6.931 \cdot 10^{-6}$	$1.772 \cdot 10^8$

Table 6: Free-stream Flow Parameters

Utilizing the **ParaView** software, the shock angle β and edge values may be obtained:

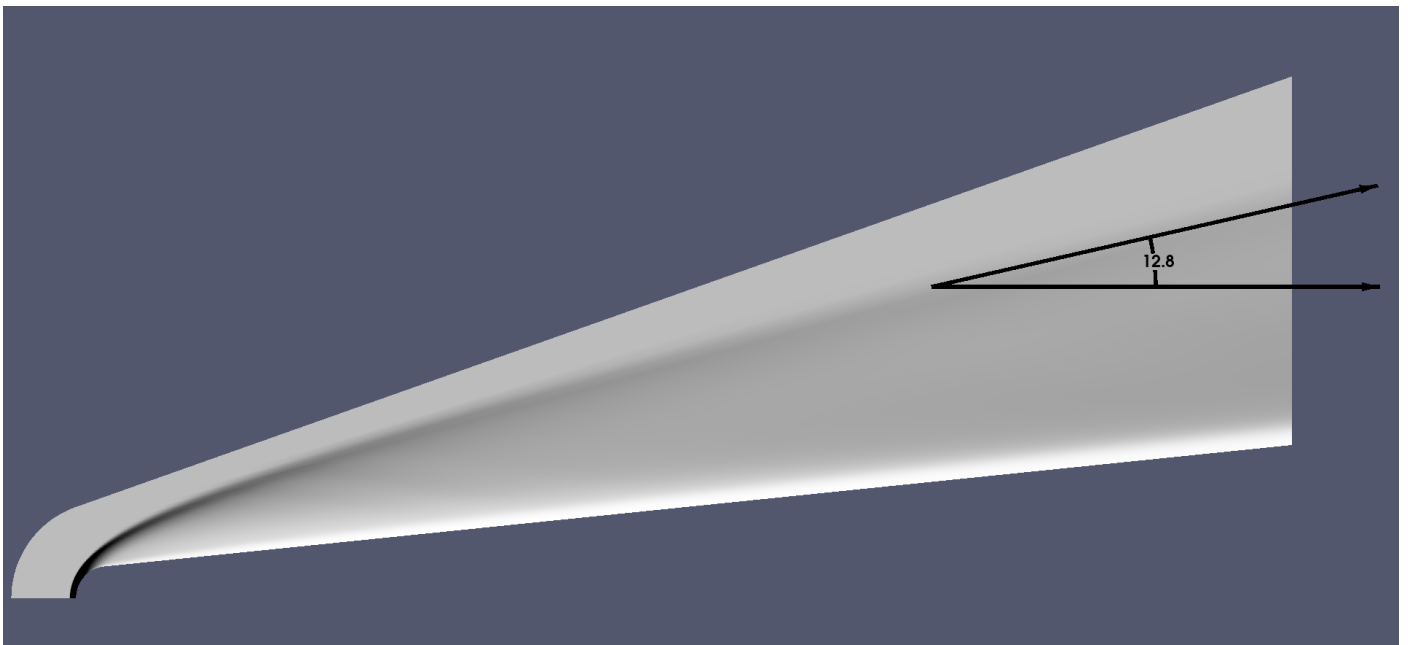


Figure 5: Shock angle $\beta[deg]$

	M_e	$\beta [deg]$	$U_e [\frac{m}{s}]$	$T_e[K]$
TM Solver	4.619	12.92°	988.6	114.0
OF Sim.	4.703	12.77°	992.1	110.7

Table 7: Boundary Edge Values

6.3.2 Consistency Along a Ray

To further verify the conical nature of the computed base flow, flow variables were sampled along a ray extending parallel to the cone surface, positioned between the viscous boundary layer and the shock. For an ideal steady conical flow, all flow quantities depend solely on the polar angle and remain constant along any such ray originating from the cone apex.

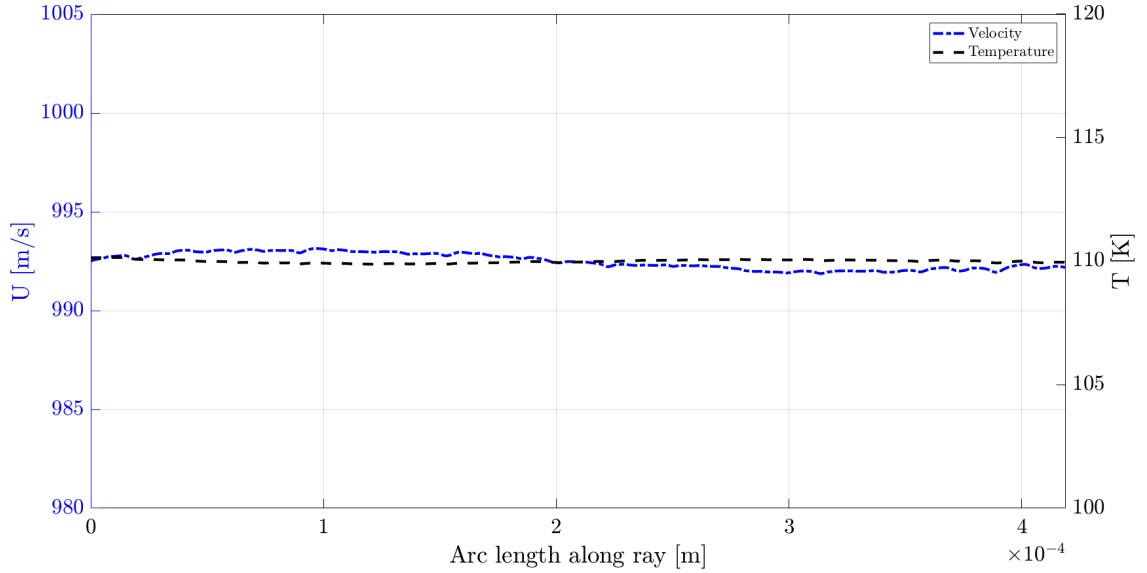


Figure 6: Variation of velocity and temperature along a ray parallel to the cone surface (between the boundary layer and the shock)

As shown in Fig. 6, the flow parameters, velocity and temperature, remain nearly constant along the selected ray, confirming that the computed flow field largely satisfies the expected *conical self-similarity*. Nevertheless, small yet measurable variations are present. These deviations, although minor relative to the overall range of the quantities, likely stem from residual numerical or grid-resolution effects. The observation suggests that while the current mesh provides an accurate representation of the global conical flow structure, additional grid refinement, particularly in the region between the boundary layer and the shock, could further minimize discretization-induced artifacts and improve local flow uniformity.

6.3.3 Boundary-Layer Velocity and Temperature Profiles

Finally, boundary-layer profiles of velocity and temperature were extracted at multiple axial locations along the cone surface. These profiles exhibit the expected physical trends: a monotonic increase in velocity from zero at the wall (no-slip condition) to the edge value U_e , and a corresponding decrease in temperature from the wall temperature T_w toward the recovery temperature at the boundary-layer edge. The gradual thickening of the boundary layer with downstream distance and the smooth variation of both quantities further confirm the numerical consistency of the solution.

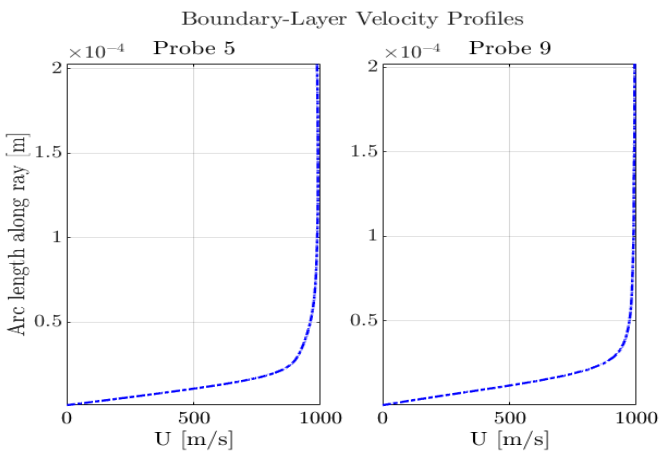


Figure 7: Boundary Layer Profiles - U (probes 5 & 9)

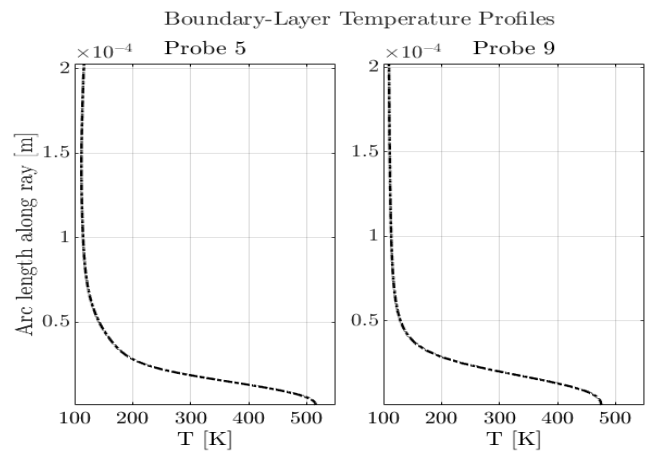


Figure 8: Boundary Layer Profiles - T (probes 5 & 9)

Collectively, the results from the grid-independence study, comparison with the TM solver, constancy along a radial ray, and the physically consistent boundary-layer development provide a comprehensive validation of the computed base flow. The agreement across all these criteria establishes that the obtained solution is both numerically stable and physically reliable, and can therefore be confidently used as the foundation for subsequent linear stability analysis.

6.4 Linear Stability Analysis

Due to the limited scope of this study, the Orr–Sommerfeld equation, a general eigenvalue equation derived from the linearised Navier–Stokes equations, is utilised to analyse the linear stability of a viscous, parallel flow and demonstrate the influence of the Reynolds number on the stability characteristics of the base flow. In this case, the base flow considered is the classical *plane Poiseuille flow*, described by the velocity profile $U(y) = 1 - y^2$ within the domain $y \in [-1, 1]$.

The Orr–Sommerfeld equation is solved numerically using the **Chebyshev collocation method**, which allows for spectral accuracy in representing the wall-normal derivatives. The eigenvalue problem is formulated as

$$\mathcal{A}\hat{\psi} = c\mathcal{B}\hat{\psi}, \quad (50)$$

where $c = c_r + ic_i$ is the complex phase velocity. The sign of c_i , determines the stability of the disturbance: $c_i < 0$ corresponds to a decaying (stable) wave, whereas $c_i > 0$ indicates exponential amplification and instability. The eigenvalue c is related to the complex frequency ω used in the general formulation of Eq. (41) through $c = \omega/\alpha$. Both forms are equivalent; a positive ω_i (temporal growth) corresponds directly to $c_i > 0$ in the Orr–Sommerfeld equation.

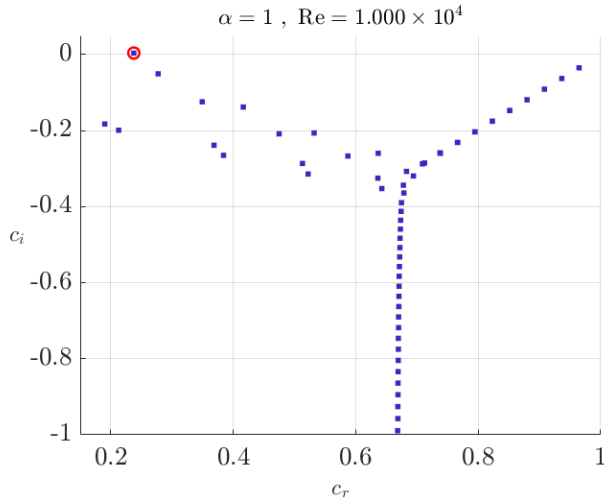


Figure 9: *Unstable* Eigenvalue Spectrum

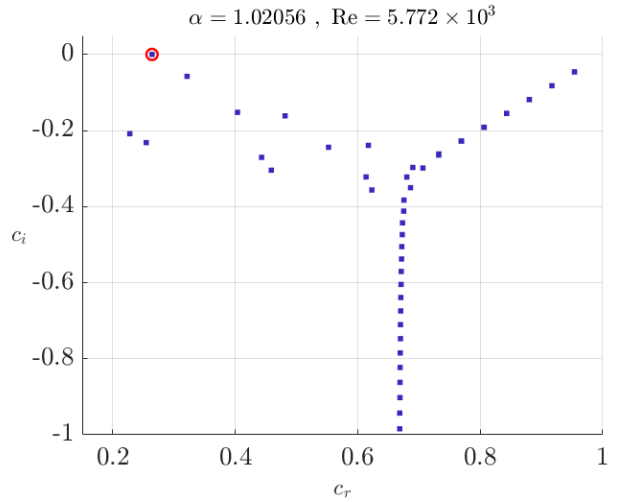


Figure 10: *Critical* Eigenvalue Spectrum

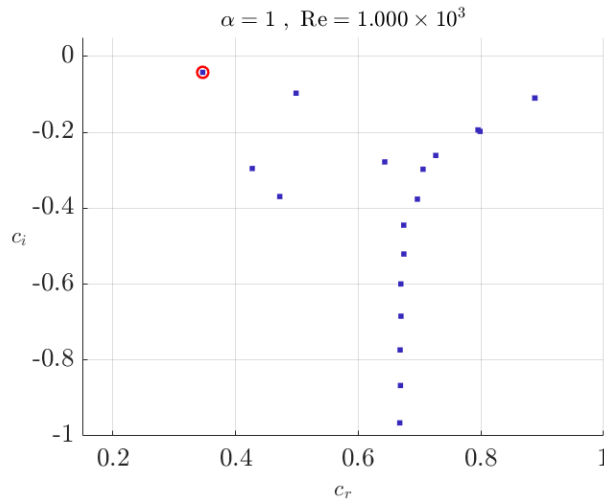


Figure 11: *Stable* Eigenvalue Spectrum. Least stable mode at $(0.3463, -4.213 \cdot 10^{-2})$

At $Re = 10^3$ (Figure 11), all eigenvalues lie below the real axis, confirming the flow is *linearly stable*. Contrastingly, when greatly increasing the Reynolds number beyond the critical threshold up to $Re = 10^4$ (Figure 9), the dominant eigenvalue crosses into the upper half of the complex plane ($c_i > 0$), signifying an exponentially growing Tollmien–Schlichting (TS) wave and confirming that the flow becomes *linearly unstable*. A point of great interest is that as the Reynolds number

increases to $Re \approx 5.772 \times 10^3$ (Figure 10), the least stable eigenvalue approaches $c_i > 0$, indicating the onset of neutral stability. This value, as well as the TS wave found at $Re = 10^4$, correspond to the values for plane Poiseuille flow first computed with spectral accuracy by Orszag (1971):

Eigenval.	Present Work ($M + 1 = 64$)	Orszag ($M + 1 = 50$)
c_i	$-3.576 \cdot 10^{-8}$	$5.9 \cdot 10^{-10}$
c_r	0.2640	0.2640

Table 8: Computed eigenval. at $\alpha = 1.0206, Re = 5772$

Eigenval.	Present Work ($M + 1 = 64$)	Orszag ($M + 1 = 50$)
c_i	$3.740 \cdot 10^{-3}$	$3.740 \cdot 10^{-3}$
c_r	0.2375	0.2375

Table 9: Computed eigenval. at $\alpha = 1, Re = 10^4$

Limitations & Improvements

The present Orr–Sommerfeld analysis constitutes a preliminary demonstration of viscous flow stability in an idealised, incompressible parallel flow. In future work, this framework will be extended to perform a **linear stability analysis of the viscous–compressible flow over a conical hypersonic vehicle**. To this end, the steady base-flow fields obtained from the *OpenFOAM* simulations presented earlier in this report will serve as the underlying mean flow on which the stability analysis is performed. This will require reformulating the governing LNSE equations in their **compressible form** and mapping them into **spherical (or conical) coordinates** to correctly capture the geometry of the cone. Because the spectral solver will operate on a collocation grid distinct from the numerical mesh, the flow variables (U, T, ρ, μ) from *OpenFOAM* will need to be **interpolated onto the spectral grid** prior to constructing the linear operators. Ultimately, this integration between the simulated base flow and the spectral stability solver will provide a comprehensive framework for predicting transition onset on conical geometry, and later, on more complex configurations, under realistic hypersonic conditions.

7 Discussion and Conclusions

This study established a validated computational framework for analyzing hypersonic flow over conical geometries, serving as a preparatory step toward future linear stability analysis. The work combined analytical, numerical, and computational methods to construct a consistent workflow: beginning with the derivation and validation of the inviscid Taylor–Maccoll (TM) formulation, followed by viscous baseflow simulations using `OpenFOAM`, and concluding with a proof of concept implementation of the Orr–Sommerfeld stability formulation.

The inviscid analysis employed the Taylor–Maccoll equations derived from the axisymmetric, inviscid compressible Navier–Stokes equations under conical similarity assumptions. The nonlinear ordinary differential equation was integrated numerically using a fourth order Runge–Kutta method combined with a shooting procedure. Validation against published data demonstrated excellent agreement across a range of Mach numbers and cone half-angles, confirming the accuracy and reliability of the solver. These results provided a theoretical reference for assessing the viscous numerical simulations.

The viscous baseflow was computed using the `rhoCentralFoam` solver in `OpenFOAM`, employing a one cell thick structured 3D mesh representing the conical geometry with a finite radius nose. To minimize grid related effects, a grid-independence study was performed under identical boundary and freestream conditions. The analysis demonstrated that the residual convergence histories and final steady-state density fields were not significantly affected by mesh refinement, indicating that the results were largely independent of the chosen grid resolution.

The validated mesh was then used to examine the main flow features. First, the detached shock structure was visualized, and the measured shock angle showed good agreement with the corresponding TM prediction. Second, a quantitative comparison between the TM solution and simulation results was conducted at the edge of the boundary layer, including the Mach number M_e , temperature T_e , and velocity U_e , all exhibiting close correspondence. Next, flow properties were sampled along a radial ray extending from the cone surface to the outer flow, confirming the near-constancy of the edge values consistent with conical similarity. Finally, boundary-layer profiles of velocity and temperature were extracted at two distinct axial locations. Both sets of profiles exhibited physically consistent behavior, with velocity increasing from the wall and the boundary layer thickening downstream. While the overall agreement with theoretical expectations was strong, the results also indicated the need for further mesh refinement to achieve higher precision and enhanced numerical stability in future simulations.

In parallel, a preliminary linear stability framework was developed as a conceptual demonstration of how the stability of the computed baseflows could later be analyzed. The linearized Navier–Stokes equations were simplified to the incompressible Orr–Sommerfeld equation, discretized using a Chebyshev collocation scheme, and solved as a generalized eigenvalue problem. The computed spectra were compared against the classical results of Orszag (1971) for plane Poiseuille flow, showing excellent agreement for both the neutral and unstable modes. This proof-of-concept successfully verified the numerical procedure and served as an introductory step toward future compressible and axisymmetric stability analyses.

Future Work

Future efforts will focus on utilizing more refined computational meshes to achieve greater numerical accuracy and improved shock and boundary-layer resolution. In parallel, the framework will be extended to perform viscous-compressible linear stability analysis directly on the `OpenFOAM` baseflows via a variety of approaches.

Further developments will primarily focus on extending the current framework to more complex geometries, particularly the cone-flare-cylinder configuration representative of the ROTEX–T model. This expansion will allow assessment of the effects of geometric discontinuities, surface curvature, and flow interaction between the cone, flare, and cylindrical afterbody on boundary-layer development and stability. Such analyses will constitute a critical step toward applying the present methodology to realistic hypersonic vehicle configurations and enabling predictive transition studies.

In summary, the present work has developed the essential components required for future stability studies of hypersonic conical flows. The combination of an analytically verified Taylor–Maccoll solver, a numerically converged viscous baseflow, and a conceptually validated linear stability framework provides a foundation for subsequent, fully coupled analyses. Building upon this groundwork, future efforts will aim to apply the developed methodology to the ROTEX–T cone-flare-cylinder configuration, enabling a detailed investigation of boundary-layer behavior and transition mechanisms in realistic hypersonic vehicle geometries and flows.

References

- Davami, J., Juliano, T. J., Scholten, A., Paredes, P., Benitez, E. K., Running, C. L., Dylewicz, K., Pezlar, V., Theofilis, V., Thiele, T., and Willems, S. (2024). Separation and transition on the rotex-t cone-flare. In *AIAA SciTech Forum*.
- DLR (2016). Roll-out of rotex-t. Image courtesy of DLR, Göttingen, Germany. © Deutsches Zentrum für Luft- und Raumfahrt (DLR).
- Dylewicz, K. (2025). *Linear Instabilities in Hypersonic Conical Flows – Stability Analysis and Advancements in Numerical Methods*. PhD thesis, University of Liverpool. PhD Thesis.
- Fedorov, A. V. (2011). Transition and stability of high-speed boundary layers. *Annual Review of Fluid Mechanics*, 43:79–95.
- González, P. P. (2014). *Advances in Global Instability Computations: From Incompressible to Hypersonic Flow*. PhD thesis, Universidad Politécnica de Madrid, Madrid, Spain. Ph.D. thesis. Available at <https://oa.upm.es/29171/>.
- Kufner, E. and Dallmann, U. (1995). Entropy- and boundary layer instability of hypersonic cone flows—effects of mean flow variations. In Matsushita, M. and et al., editors, *Laminar-Turbulent Transition: IUTAM Symposium, Sendai/Japan, September 5–9, 1994*, pages 197–204. Springer.
- Mack, L. (1969). Boundary layer stability theory. Technical Report Report 900-277, Jet Propulsion Laboratory.
- Mack, L. (1984). Boundary-layer linear stability theory. Technical Report AGARD Report No. 709, Advisory Group for Aerospace Research and Development (AGARD).
- Malik, M. R. (1990). Numerical methods for hypersonic boundary layer stability. *Journal of Computational Physics*, 86(2):376–413.
- Morkovin, M. V., Reshotko, E., and Herbert, T. (1994). Transition in open flow systems—a reassessment. *Bulletin of the American Physical Society*, 39:1882. APS Division of Fluid Dynamics; often cited for the transition “roadmap” diagram.
- Orszag, S. A. (1971). Accurate solution of the orr–sommerfeld stability equation. *Journal of Fluid Mechanics*, 50(4):689–703.
- Pezlar, V. (2024). Taylor–maccoll solver (version 3). Numerical implementation for solving inviscid conical flow via the Taylor–Maccoll formulation.
- Schlichting, H. (1933). Über die entstehung der turbulenz bei der laminaren strömung entlang einer platte. *Nachrichten von der Gesellschaft der Wissenschaften zu Göttingen, Mathematisch-Physikalische Klasse*, pages 181–208. Translated as “Concerning the Origin of Turbulence in the Laminar Boundary Layer,” NACA TM-823, 1936.
- Schmisseur, J. D. (2015). Hypersonics into the 21st century: A perspective on afosr-sponsored research in aerothermodynamics. *Progress in Aerospace Sciences*, 72:3–16.
- Schneider, S. P. (2008). Effects of high-speed tunnel noise on laminar-turbulent transition. *Journal of Spacecraft and Rockets*, 45(2):193–209.
- Stetson, K., Kimmel, R., Donaldson, J., and Siler, L. (1983). A comparison of hypersonic boundary-layer stability theory with experiment on cones at mach 8, 10, and 11. In *AIAA 16th Fluid and Plasma Dynamics Conference*, Danvers, MA. AIAA.
- Theofilis, V. (2011). Global linear instability. *Annual Review of Fluid Mechanics*, 43:319–352.
- Tollmien, W. (1929). Über die entstehung der turbulenz. *Nachrichten von der Gesellschaft der Wissenschaften zu Göttingen, Mathematisch-Physikalische Klasse*, pages 21–44. Translated as “On the Origin of Turbulence,” NACA TM-609, 1931.